Numerical Simulation of Long Wave Run-up for Breaking and non-Breaking Waves

Mostafa S. Shadloo[1,], Robert Weiss[2], Mehmet Yildiz[3], Robert A. Dalrymple[4]*

1. LHEEA Lab., Ecole Centrale de Nantes, CNRS / UMR-6598, Nantes, France
2. Department of Geosciences, Virginia Tech., Blacksburg, VA, USA
3. Faculty of Engineering and Natural Sciences, Sabanci University, Istanbul, Turkey
4. Department of Civil Engineering, Johns Hopkins University, Baltimore, MD, USA

ABSTRACT

Tsunamis produce a wealth of quantitative data that can be used to improve tsunami hazard awareness and to increase preparedness of the population at risk. These data also allow for a performance evaluation of coastal infrastructure and observations of sediment transport, erosion and deposition. The interaction of the tsunami with coastal infrastructures and with the movable sediment bed is a three-dimensional process. Therefore, for run-up and inundation prediction, three-dimensional numerical models must be employed. In this study, we have employed Smoothed Particle Hydrodynamics (SPH) to simulate tsunami run-up on idealized geometries for validation and exploring three-dimensional flow structures in tsunamis. We make use of the canonical experiments for long-wave run-up for breaking and non-breaking waves. The results of our study prove that SPH is able to reproduce the run-up of long waves for different initial and geometric conditions. We have also investigated the applicability and the effectiveness of different viscous terms that are available in SPH literature. Additionally, a new breaking criterion based on numerical experiment is introduced and its similarities and differences with existing criteria are discussed.

KEYWORDS: Smoothed Particle Hydrodynamics (SPH), Particle Methods, CUDA GPU, Solitary Wave, Tsunami, Sub Particle Scales (SPS) Turbulence.

INTRODUCTION

Large traveling water waves over the ocean, usually caused by earthquakes, submarine landslides, or volcanic eruptions, are known as tsunamis. Tsunamis have been causing considerable widespread damage and loss human of lives. Since tsunamis are characterized as water waves with long periods and wavelengths, for the research application, it is practical to consider them as solitary waves. These waves near the coastal area are usually investigated analytically using either Boussinesq or shallow-water-wave equation. The Boussinesq approximation is valid for weakly-nonlinear and long water waves. The set of equations for the later approach can be directly derived from the former ones by neglecting the dispersion effects and the vertical accelerations. Both sets of equations are characterized by the high wave length to water depth ratio. Shallow water waves have been studied through laboratory experiments for decades (Synolakis (1987); Pedersen & Gjevik (1983)). Also, elegant analytical solutions of the shallow water equations were developed by Synolakis (1987) and Pedersen & Gjevik (1983). As in the case of any other wave, the solitary waves can break. Although breaking and nonbreaking waves have been extensively studied in the laboratory (Synolakis (1986, 1987); Pedersen & Gjevik (1983)), the theoretical understanding of breaking solitary waves is incomplete because of the limiting boundary and initial conditions that are necessary to find a meaningful analytical solution. Even though the shallow-water type of equations can incorporated with higher-order derivatives to simulate dispersion and other nonlinearities, their results are mainly limited by some critical assumptions such as two-dimensionality. In the last two decades, the SPH method has become an important tool in outreach efforts and testing future engineering designs as well as in tsunami research. Extensive SPH simulations have been conducted in order to study the dynamic behaviors of such waves (Landrini et al. (2007), Khayyer et al. (2008)). Nevertheless, most of the available SPH simulations in literature are two-dimensional and the effects of viscosity and/or turbulent viscosity are neglected. The simulation of nonbreaking and breaking solitary waves with three-dimensional numerical models offers an alternative approach to explore the linear and nonlinear physical processes occurring during near-shore propagation, run-up and withdrawal of solitary waves. Recent developments in computer technology and the better understanding of numerical methods have provided the opportunity to carry out massively parallel simulations of fluid mechanics on a very small scale. Hence, it is possible to solve the fully three-dimensional Navier-Stokes equations. Here, we have employed a three-dimensional Lagrangian approach to simulate the dynamics of breaking and nonbreaking solitary waves thereby introducing some new insights about the behavior of these waves.

GOVERNING EQUATIONS

The governing equations employed in our modeling efforts are the conservation of mass and momentum equations, which are written in the Lagrangian form as:

$$\frac{D\rho}{Dt} = -\rho\,\nabla \cdot \vec{u}\,, \tag{1}$$

$$\frac{D\vec{u}}{Dt} = -\frac{\nabla p}{\rho} + \nu\,\nabla^2\vec{u} + \vec{g}\,, \tag{2}$$

wherein $\vec{u}$ is the velocity vector, p is the pressure, t is the time, ρ is the density, $\vec{g}$ is the gravitational acceleration vector, ν is the laminar

* Corresponding Author: Mostafa S. Shadloo (email: msshadloo@ec-nantes.fr)

kinematic viscosity and $D/Dt = \partial/\partial t + \vec{u} \cdot \nabla$ is the material time derivative operator.

Nonlinearities in fluid flow generate hydrodynamic instabilities that cause the generation of coherent structures and other turbulent features. To adequately take turbulence and the dissipation of turbulent energy across a wide spectrum of spatial scales into account, two avenues can be taken, namely, Direct Numerical Simulations (DNS), and averaging techniques to dissipate turbulent energy that is of a subgrid spatial size. One example for the averaging technique is Large Eddy Simulation (LES), which features a filter technique for subgrid turbulence, but is capable of resolving larger scale turbulent features. For the SPH method, a spatial filter is applied on Eqs. (1) and (2). Then, the governing equations for the particle scale (PS) in Lagrangian representation (similar to grid scale in Eulerian representation) can be introduced as:

$$\frac{D\rho}{Dt} = -\rho \, \nabla \cdot \vec{\bar{u}} \,, \tag{3}$$

$$\frac{D\vec{\bar{u}}}{Dt} = -\frac{\nabla \bar{p}}{\rho} + \vec{g} + v \, \nabla^2 \vec{\bar{u}} + \frac{\nabla \cdot \boldsymbol{\tau}^*}{\rho} \,, \tag{4}$$

where the over bar symbol '-' denotes mean or particle scaling component, and

$$\boldsymbol{\tau}^* = \rho \left(2v_t \overline{\boldsymbol{S}} - \frac{2}{3} \text{tr}(\overline{\boldsymbol{S}})\overline{\boldsymbol{I}} \right) - \frac{2}{3} \rho C_I \Delta^2 \, \overline{\boldsymbol{I}}, \tag{5}$$

is the turbulent stress tensor representing the interaction of the unresolved small motions or the sub particle scales (SPS) on the resolved large particle scales. In Eq. (5), Δ is the initial particle spacing and $\overline{\boldsymbol{I}}$ is the identity tensor. The eddy viscosity v_t is calculated from the standard Smagorinsky model as

$$v_t = (C_s\Delta)^2 |\overline{\boldsymbol{S}}| \,, \tag{6}$$

in which $|\overline{\boldsymbol{S}}| = (2\overline{\boldsymbol{S}}:\overline{\boldsymbol{S}})^{0.5}$ is the local strain rate, and $\overline{\boldsymbol{S}}$ is the deformation rate tensor defined as

$$\overline{\boldsymbol{S}} = \frac{1}{2}\left(\nabla\vec{\bar{u}} + \left(\nabla\vec{\bar{u}}\right)^T\right), \tag{7}$$

The C_I and C_s are empirical constant with as $C_I = 6.6 \times 10^{-4}$ and $C_s = 0.12$ (Blinn et al. (2002); Dalrymple & Rogers (2006)).

SMOOTHED PARTICLE HYDRODYNAMICS

Being successful in simulating various fluid mechanics applications within the last decade, SPH has received increased attention among the meshless approaches. Owing to its Lagrangian nature, it has unique advantages to deal with fast flow dynamics problems (i.e., no convective term in momentum equation). Additionally, being a member of meshless particle family, fluid flows with large deformations, interfaces and free surfaces can be treated inherently in a relatively easy manner (Zainali et al., 2013). In this method, particles refer to integration point, which carry all hydrodynamic properties and can move freely. The hydrodynamics properties of a given particle are calculated from weighted contributions of neighboring particles through using a weighting/kernel function. Neighboring particles include those that are in the environs of the base particle, called compact support domain. The integral estimate or the kernel approximation for an arbitrary function $f(\vec{r}_i)$ can be introduced as (Monaghan, 1992)

$$f(\vec{r}_i) \cong \langle f(\vec{r}_i) \rangle \equiv \int_\Omega f(\vec{r}_i)W(r_{ij},h)d^3r_j \,, \tag{8}$$

where $W(r_{ij},h)$, here after represented by W_{ij}, is a smoothing or kernel function, the angle bracket $\langle \ \rangle$ denotes the kernel approximation and the length h defines the supporting domain of the particle of interest. Apparently, the type of kernel function and the smoothing length are two important input parameters that control the accuracy and computational costs of the SPH method. Here, r_{ij} is the length of the distance vector $(\vec{r}_{ij} = \vec{r}_i - \vec{r}_j)$ between the particle of interest i and its neighboring particles j and $\vec{r}_i$ and $\vec{r}_j$ are the position vectors for particles i and j, respectively.

Replacing the integration in Eq. (8) with SPH summation over N neighboring particles j and setting $d^3r = m_i/\rho_i$, one can write SPH interpolation for an arbitrary field f_i as

$$f_i = f(\vec{r}_i) = \sum_j \frac{m_j}{\rho_j} f_j W_{ij}, \tag{9}$$

The SPH approximation for the gradient of the same function can be introduced as

$$\nabla f_i = \sum_j \frac{m_j}{\rho_j}\left(f_j - f_i\right)\nabla_i W_{ij} \,, \tag{10}$$

or in the conservative way as

$$\nabla f_i = \sum_j m_j \left(\frac{f_i}{\rho_i^2} + \frac{f_j}{\rho_j^2}\right)\nabla_i W_{ij} \,. \tag{11}$$

It is noted that the above equation is asymmetric with respect to particles i and j. Following the Monaghan (1992), the laminar viscous term in the linear momentum balance equation is represented by

$$v \, \nabla^2\vec{\bar{u}}_i = \sum_j m_j \frac{4v}{(\rho_i + \rho_j)} \frac{\vec{r}_{ij}\cdot\nabla_i W_{ij}}{r_{ij}^2} \vec{\bar{u}}_{ij} \,. \tag{12}$$

Throughout the present simulations, the compactly supported three-dimensional Wendland kernel function is used, which are given in the form of (Wendland, 1995)

$$W_{ij} = \alpha \left(1 - \frac{q}{2}\right)^4 (2q + 1), \ \ q < 2 \,, \tag{13}$$

where $\alpha = 15/(16\,\pi h^3)$ for 3-D simulations and q is defined as $q = r_{ij}/h$.

Applying discrete SPH formulations to the governing equations, the continuity and momentum balance equations can be expressed as,

$$\frac{D\rho_i}{Dt} = \sum_j m_j\left(\vec{\bar{u}}_i - \vec{\bar{u}}_j\right)\cdot \nabla_i W_{ij} \,, \tag{14}$$

$$\frac{D\vec{\bar{u}}_i}{Dt} = \tag{15}$$
$$\sum_j m_j \left(\frac{\bar{p}_i}{\rho_i^2} + \frac{\bar{p}_j}{\rho_j^2}\right)\nabla_i W_{ij} + \vec{g} + \sum_j m_j \frac{4v}{(\rho_i + \rho_j)}\frac{\vec{r}_{ij}\cdot\nabla_i W_{ij}}{r_{ij}^2}\vec{\bar{u}}_{ij} +$$
$$\sum_j m_j \left(\frac{\tau_i^*}{\rho_i^2} + \frac{\tau_j^*}{\rho_j^2}\right)\cdot \nabla_i W_{ij} \,.$$

The numerical scheme used here is the predictor-corrector scheme introduced by Monaghan (1989). In the current work, an open source massively parallel computing C + + code, so called GPUSPH, is used. GPUSPH (www.gpusph.org) computes the three main components of the SPH method, namely, neighbor list construction, force computation, and the integration of the equation of motion, on a Graphical Processing Unit (GPU) using the Compute Unified Device Architecture (CUDA) developed by Nvidia. Further details on the discretization of model equations and its CUDA implementation can be found in the work of Herault et al. (2010).

| Table 1: Sensitivity of the numerical solutions to the particle resolution evaluated based on Run-up.					
	very coarse	coarse	medium	fine	very fine
Initial particle spacing, Δ (m)	0.03	0.025	0.02	0.015	0.01
Total number of particles	24976	40080	75435	164322	505419
Simulation time (s)	1.88×10^2	2.76×10^2	5.47×10^2	1.67×10^3	8.15×10^3
Maximum relative wave run-up, R/D	0.2775	0.3132	0.3221	0.3287	0.3245
Error with respect to the last column, %	14.48	3.47	0.77	1.31	-
Error with respect to the next succeeding column, %	11.41	2.72	2.05	1.31	-
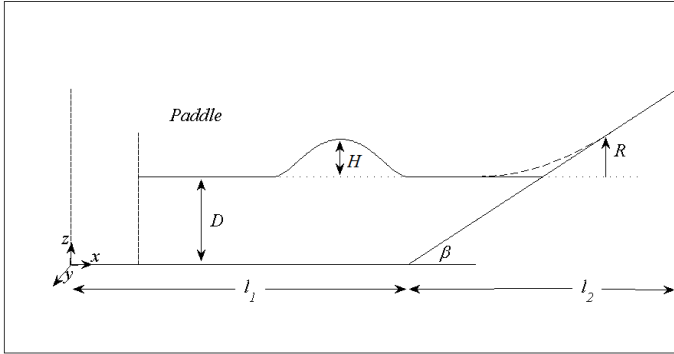
Fig. 1: 2D sketch of three dimensional numerical simulations.

PROBLEM SETUP

The geometrical setup for the long-wave experiments features a constant depth section that is followed by a sloping beach. Fig. 1 depicts the geometric setting of the long-wave run-up problem. Parameter l_1 represents the length of the constant depth part, while l_2 denotes the projected length of the sloping beach. The slope is β. The length of the setup is L = $l_1 + l_2$. The height is chosen in a way that the maximum run-up R does not exceed the height of the setup (the run-up is estimated with run-up laws provided later). Length L is a function of the slope angle and the water depth D. The width of the computational domain is constant for all test cases at $W = 0.4(m)$. The origin of the coordinate system ($x = 0$, $y = 0$ and $z = 0$ (m)) is located at the far left end. Waves are generated by a piston wave maker located near the left edge.

To generate long waves with the shape of

$$\eta(x,t) = H \operatorname{sech}^2[k(Ct - x_o)] , \tag{16}$$

we employ the wavemaker function:

$$x_o(t) = \frac{H}{kD}\tanh[k(Ct - x_o)] , \tag{17}$$

which is similar to the one suggested by Goring (1978). Here, $k = \sqrt{3H/4D^3}$, $C = \sqrt{g(D + H)}$, and H is the desired wave amplitude.

Sample position and velocity of the piston for the relative wave height $H/D = 0.1$ and still-water level of $D = 0.4$ (m) are shown in Fig.2. As can be seen in this figure, the trajectory of the paddle is such that it can produce a perfect solitary wave with a desirable wave height.

RESULTS

In this study, the density and the kinematic viscosity of the fluid are set to $\rho = 1000$ (kg/m^3) and $v = 10^{-6}$ (m^2/s), respectively. The gravitational force $\vec{g}$ acts only in downward direction (z direction) on all particles with the numerical value of $g = 9.81$ (m/s^2). The slope β ranges from 2.88º to 30º. The SPS turbulent model is employed in all test cases unless stated otherwise.
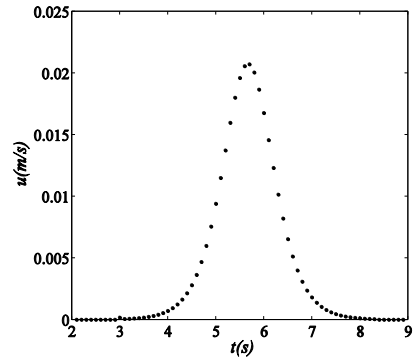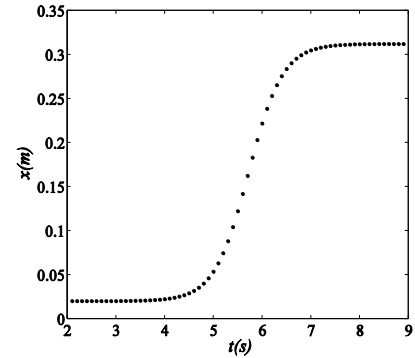

Fig. 2: Sample position (up) and velocity (down) of the paddle.

The boundaries are treated as solid walls, and the no-slip and zero pressure gradient boundary conditions are imposed using the Monaghan-Kajtar method (Monaghan & Kajtar (2009)). In the SPH method, particles may tend to readjust their initial positions giving rise to spurious current generally in regions where the kernel is truncated, i.e. near solid boundaries and free surfaces (Monaghan(1994); Colagrossi et al. (2012)). At initial time steps, this situation may result in unwanted disturbances in the water column and the free surface. To circumvent such effects, we have waited for three seconds before the wave maker starts to move.

We have performed a limited parameter study comprising more than 50 individual simulations. To investigate the sensitivity of the numerical solutions to the number of particles, the relative maximum run-up (R/D) for a slope of $\beta = 20^o$ with $H/D = 0.1$ and $D = 0.4$ (m) is computed for the very coarse ($\Delta = 0.03$ (m)), coarse ($\Delta = 0.025$ (m)), medium ($\Delta = 0.02$ (m)), fine ($\Delta = 0.015$ (m)) and very fine ($\Delta = 0.010$ (m)) particle spacing. In this work, the maximum run-up height is defined as the y-position of a particle having the largest x-position provided that the particle in question has a prescribed number of neighbors thereby excluding free-surface particles isolated from the fluid body completely. This predefined neighbor number is dependent on simulation parameters such as beach angle, wave height, among others (i.e., in this study, it is around 10 particles, which is determined through conducting several test simulations and visually monitoring the run-up distance).
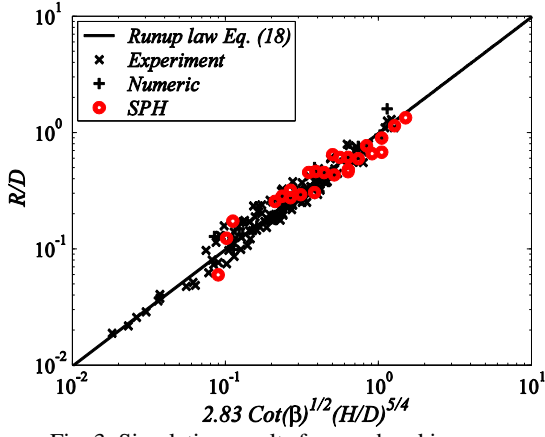
Fig. 3: Simulation results for non-breaking waves.

$$R/D = 2.83\ Cot(\beta)^{0.5}\ (H/D)^{1.25}\ . \tag{18}$$

Fig.3 shows the relative maximum run-up of solitary waves climbing up on different beaches versus the normalized wave height. The numerical results of the current simulations plotted in this figure are summarized in Table 2. Close agreement among the run-up law equation (Eq. 18), selected experimental data (originally collected in Table T3.2 by Synolakis (1986)), numerical calculations of (Pedersen & Gjevik (1983); Heitner & Housner (1970); Kim et al. (1983)) and the current simulation results is observed.

Increasing the wave height changes the regime of flow from the non-breaking solitary wave to the breaking ones. Pedersen & Gjevik (1983) suggested that the waves break when

$$H/D = 0.8183\ Cot(\beta)^{-10/9}\ , \tag{19}$$

Later, based on nonlinear analysis, Synolakis (1986) developed the following weaker restriction

$$H/D = 0.479\ Cot(\beta)^{-10/9}\ . \tag{20}$$

Eq. (19) differs from Eq. (20) due to the fact that the first one indicates the border for the wave height at which a solitary wave breaks during the washback while the second criterion shows the limit at which a solitary wave first breaks during the run up. Stating otherwise, the wave that has not been broken during run up might get broken during the washback. However, both criteria indicate that with increasing beach angle β and/or still water height D, the system will have more non-breaking waves.

Synolakis (1987), based on laboratory beach findings, reported that washback waves break at $H/D > 0.044$ and a break during run up occurs when $H/D > 0.055$, which are different from the values calculated using Eqs. (19) and (20), respectively. The main reason for the differences between the theory and experimental results is that the analytical solution for modeling run-up is based on shallow-water-wave formulas that involve several simplifications. Furthermore, he mentioned that the asymptotic result from the run-up law (Eq. (18)) is also valid for all waves, which first break during the washback. However, for the run-up breaking waves, he reported the correlation

$$R/D = 1.109\ (H/D)^{0.583}\ , \tag{21}$$

Table 1 shows the convergence study based on relative maximum wave run-up. It is found that for a very coarse spacing, the run-up over offshore depth ratio, R/D, has an approximately 15 % error in comparison to the one obtained by the very fine particle spacing. This error decreases down to 2 % for the medium particle spacing. Also given in the table is the amount of time needed to simulate one second of real time in the model. There is an order of magnitude difference between the very coarse and the finest particle spacing test cases. It seems that the medium spacing represents a good trade-off between accuracy and computational cost. Therefore, intermediate particle number is chosen for numerical simulations presented in this study (*i.e.* $\Delta = 0.02$ (m)). It is noted that simulations are performed on a single Nvidia Tesla M2075 device with 448 CUDA core and Linux (64 bit) operating system.

For practical reasons, the wave run-up is an important measure for solitary waves on a sloping beach. Depending on the water height, wave amplitude, and the angle of the sloping beach, the run-up is different for breaking and nonbreaking waves. Synolakis (1987) derived the following run-up law for nonbreaking waves:

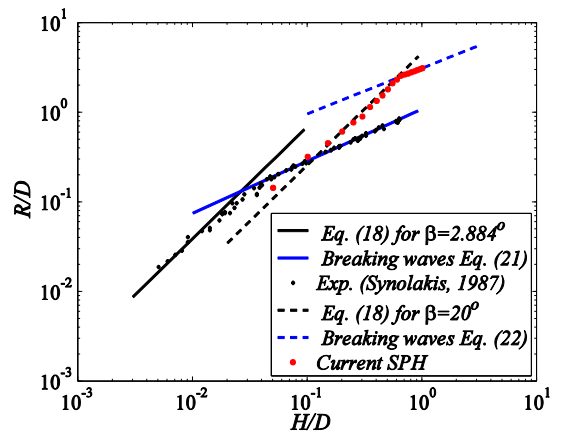| Table 2: Reported test cases for non-breaking waves.			
H/D	β	$D\ (m)$	R/D
0.019	2.884	0.31	0.0603
0.021	2.884	0.2914	0.1246
0.1	10	0.4	0.3077
0.15	10	0.4	0.4837
0.2	10	0.4	0.6637
0.1	15	0.4	0.2947
0.15	15	0.4	0.4357
0.2	15	0.4	0.6012
0.05	20	0.4	0.1745
0.1	20	0.4	0.3221
0.15	20	0.4	0.4582
0.2	20	0.4	0.6172
0.25	20	0.4	0.7772
0.3	20	0.4	0.9063
0.35	20	0.4	1.1552
0.4	20	0.4	1.3531
0.1	20	0.2	0.2781
0.2	20	0.2	0.4645
0.3	20	0.2	0.6835
0.1	25	0.4	0.2861
0.15	25	0.4	0.4673
0.2	25	0.4	0.6172
0.1	30	0.4	0.2583
0.15	30	0.4	0.4583
0.2	30	0.4	0.6515

Fig. 4: Relative maximum run-up as a function of relative wave amplitude for both breaking and non-breaking waves.

for the relative maximum run-up. Referring to Fig.4, our numerical

simulations indeed generate a similar behavior as elaborated above, but the values of the relative wave amplitude obtained numerically for breaking waves are somewhat higher than those of the experiment. These values are $H/D > 0.2$ and $H/D > 0.6$ for the waves that break during washback and run-up respectively. These discrepancies can be attributed to difference in the angle of sloping beach for the experimental and current numerical studies. Furthermore, it can be seen from Fig.4 that the numerically calculated R/D values are quite well represented by the run-up law in Eq.(18) up to $H/D < 0.6$ (recall that the waves with $H/D < 0.6$ does not break during the run-up). We also found that the correlation

$$R/D = 3.149\,(H/D)^{0.51}\,, \tag{22}$$

is well representative for run-up breaking waves (i.e. $H/D > 0.6$) on the numerical beach. Since the current numerical simulations have both higher beach angle β and still water height D, they contain more non-breaking waves. Therefore, waves for numerical experiments first break during the run-up at higher relative wave amplitudes H/D confirming the analytical solutions in Eqs. (19) and (20).

Although a change in slope appears in a higher relative wave amplitude H/D, it can be seen from Fig. 4 that the two correlations for the breaking waves (Eqs. (21) and (22)) are almost parallel to each other and the curves follow the same behavior meaning that this slope change appears at the transition region from the non-breaking to breaking waves. Fig.5 illustrates the simulated run-up and washback of a solitary wave with the relative wave amplitude of $H/D = 0.65$ and $D = 0.4$ (m). As seen in this figure, as the wave is reaching the inclined beach, a fluid jet start to appear on the highest part of it (refer to dimensionless times $t^* = 18.161$ and $t^* = 19.047$). This jet impinges on the tail of the front wave body and it breaks first during the run-up (refer to dimensionless times $t^* = 19.932$ and $t^* = 20.818$). At this time step strong transport of momentum takes place and turbulent mixing of energy occurs. Afterwards fluid continues to run-up. Breaking the waves during the run-up and turbulent diffusion of energy due to the eddy viscosity is the main reason for the slope change appeared in Fig. 4. Since some portions of energy are diffused, the wave has a less energy compared to the initial energy induced to the flow by the wave maker, so it climbs less height than the run-up law predicts.

In later times, a steep front develops during the washback (refer to dimensionless times $t^* = 27.905$ and $t^* = 28.791$). Due to the high kinetic energy, the wash-backed fluid pushes the bulk fluid back near the plate and creates a roll up that entraps air inside it and collapses after the second impinging (refer to dimensionless times $t^* = 29.677$ and $t^* = 30.653$). Meanwhile and till the end of the backwash the flow feels the intense turbulent mixing of energy (refer to dimensionless times $t^* = 31.499$ and $t^* = 32.335$).

To assess the importance of the turbulent mixing and the eddy viscosity dissipation, it is important to investigate the shortcomings of the inviscid and/or laminar viscosity formulas if relevant. Table 3 compares the result of the relative maximum run-up, the maximum velocities (u_{max}), and vorticities (ω_{max}) obtained using three different viscosity formulas, namely SPS turbulence viscosity (SPS-Vis), artificial viscosity (Art-Vis), and kinematic viscosity (Kin-Vis). Here, it should be noted that the vorticity is computed throughout the whole computational domain and its maximum value is reported in Table 3. For the Kin-Vis model, the values of the flow Reynolds number are 56×10^3, 72×10^4, and 18×10^5 for three different H/D values given in Table 3, respectively, which are calculated based on the characteristic scales of maximum velocity and the wave amplitude as $Re = H u_{max}/\nu$. It can be seen from the Table 3 that the Kin-Vis always produces closer results to SPS-Vis in comparison to the Art-Vis in terms of relative maximum run-up. Due to its highly

diffusive nature, the Art-Vis formulation (Monaghan, 1992) always predicts the smallest R/D values even for a very small artificial viscosity coefficient (here $\alpha = 0.01$ is used). However, the Kin-Vis appears to be over predicting the values of the maximum velocities and the vorticities with respect to the SPS-Vis except the non-breaking wave (i.e., $H/D = 0.1$). This discrepancy comes from the fact that in Kin-Vis formulation, there is less amount of dissipation compared to the SPS-Vis, which is equal to the turbulent eddy viscosity. The discrepancy becomes more evident for the higher values of initial relative wave height, especially for those that cause air entrainment in the breaking waves. It is noted from the table that in comparison to the SPS-Vis, the Art-Vis always underestimates the maximum values of velocities and vorticities while Kin-Vis overestimates these values. Since the SPS modeling depends more on the properties of flow rather than the fluid, unlike Kin-Vis and Art-Vis, one may expect that this model increase the accuracy of the SPH method especially in higher Reynolds number. Finally, it is further noted that except values with asterisk *, all maximum velocities and vorticities occurred during the backwash step of the wave breaking phenomena.

CONCLUSION

An SPH method GPUSPH has been used to study the long wave run-up of breaking and non-breaking solitary waves. Three-dimensional numerical simulations were performed for numerous beach angle and initial dimensionless wave height. Simulation results are observed to be in good agreement with those corresponding to analytical solutions and experimental data in terms of maximum run-up. Having more non-breaking waves, it is illustrated that a change in slope in maximum run-up plots appears at higher values for higher beach steep angle. Additionally the effect of different viscosity terms is investigated. It is further observed that the use of an appropriate turbulent modeling in violent flows can improve the accuracy of the results especially for higher wave amplitudes and in turn for higher Reynolds numbers.

REFERENCES

Blinn, L., Hadjadj, A., Vervisch, L., (2002), Large eddy simulation of turbulent flows in reversing systems. In: Vuillermoz, P., Comte, P., Lesieur (Eds.), Selected Proc. of the 1st French Seminar on Turbulence and Space Launchers. CNES, Paris.

Colagrossi, A., Bouscasse, B., Antuono., M., Marrone, S. (2012), Particle packing algorithm for SPH schemes, Computer Physics Communications, (183) 1641-1653.

Dalrymple, R.A., Rogers, B.D., (2006), Numerical modeling of water waves with the SPH method, Coastal Engineering (53) 141–147.

Heitner, K.L., Housner, G.W. (1970) Numerical model for tsunami runup, Proc. ASCE WW3, 701-719.

Herault, A., Bilotta, G., Dalrymple, R.A. (2010) SPH on GPU with CUDA, Journal of Hydraulic Research, (48) 74–79.

Khayyer, A., Gotoh, H., Shao S.D., (2008), Corrected Incompressible SPH method for accurate water-surface tracking in breaking waves, (55) 236–250.

Kim, S.K., Liu, P.L-F., Liggett, J.A., (1983) Boundary integral equation solutions for solitary wane generation, propagation and run-up, Coastal Engineering, (7) 299-317.

Landrini, M., Colagrossi, A., Greco, M., Tulin, M.P., (2007), Gridless simulations of splashing processes and near-shore bore propagation, Journal of Fluid Mechanics, (591) 183-213.

Monaghan, J.J., (1992) Smoothed particle hydrodynamics. Annual Review of Astronomy and Astrophysics, 1992 (30) 543–574.

Monaghan, J.J. (1989) On the problem of penetration in particle methods.Journal of Computational Physics, (82) 1– 15.

Monaghan, J.J., Kajtar, J., (2009) SPH particle boundary forces for arbitrary boundaries, Computer physics communications 180, 1811-1820.

Pedersen, G., Gjevik, B., (1983) Run-up of solitary waves, Journal of Fluid Mechanics, (135) 283-299.

Synolakis, C. E., (1986), The Runup of long waves, PhD thesis.

Synolakis, C.E., (1987), The Runup of solitary waves, Journal of Fluid Mechanics, (185) 523-545.

Wendland, H., (1995), Piecewise polynomial, positive definite and compactly supported radial functions of minimal degree, Adv. Comput. Math., (4) 389–396

Zainali, A., Tofighi, N., Shadloo, M.S., Yildiz, M., (2013), Numerical investigation of Newtonian and non-Newtonian multiphase flows using ISPH method, Computer Methods in Applied Mechanics and Engineering, 254, 99-113.

Table 3: The comparison of maximum relative run-up, velocities, and vorticities for three different viscosity formulas.

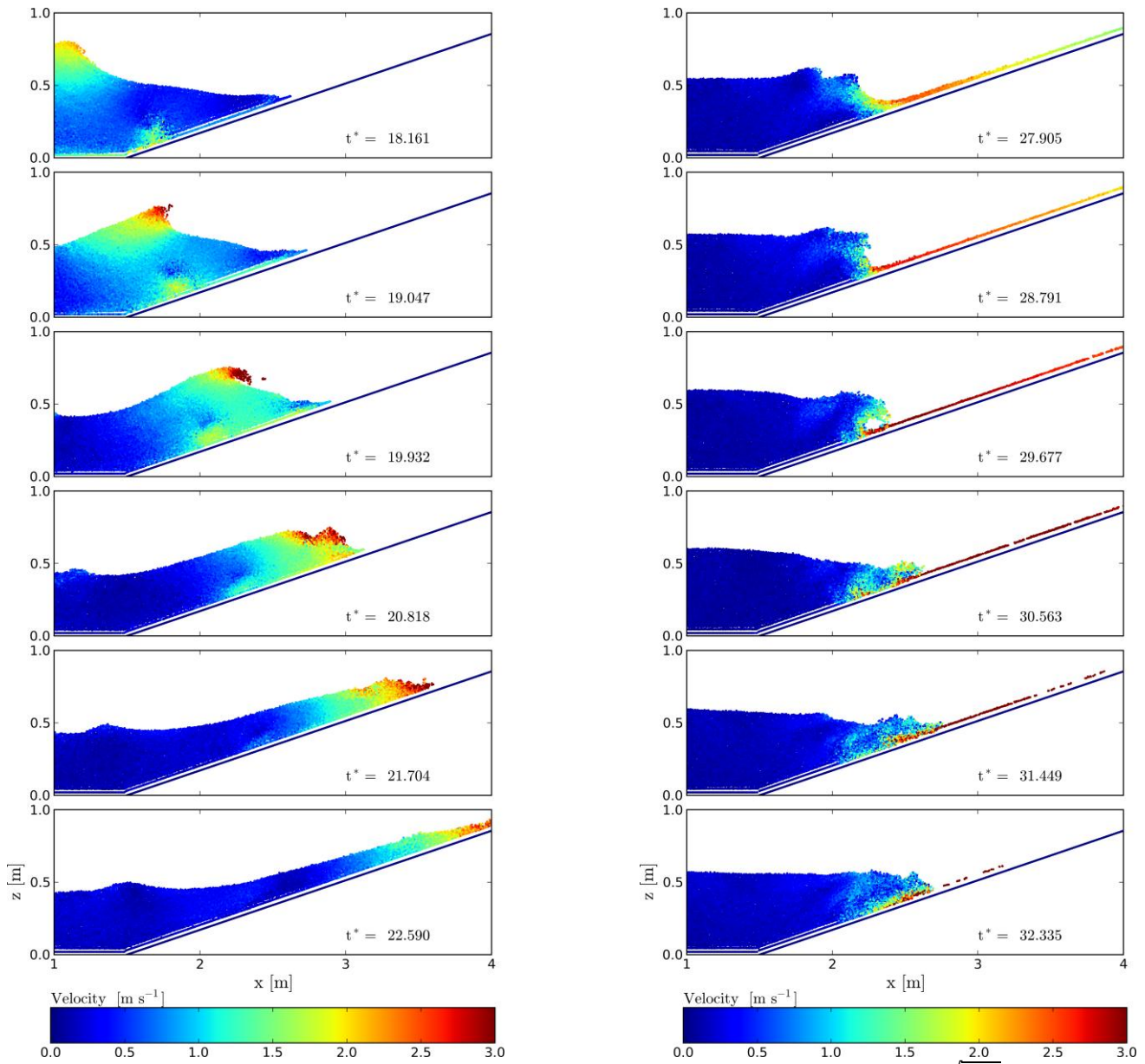| H/D	R/D			u_{max}			ω_{max}		
	0.1	0.25	0.5	0.1	0.25	0.5	0.1	0.25	0.5
SPS-Vis	0.322	0.777	1.817	2.049	3.982	4.793	53.689	120.45	175.18
Art-Vis	0.302	0.706	1.597	1.098*	2.812	8.986	18.053	90.448	166.11
Kin-Vis	0.314	0.783	1.838	1.396*	7.197	9.139	42.342	170.41	324.13

Fig. 5: Time evolution of a breaking wave during run-up (left) and washback (right). Here $t^* = t\sqrt{g/H}$.